Evaluation of Planar 3D Electrical Capacitance Tomography: from Single-Plane to Dual-Plane Configuration

Hsin-Yu Wei[1,2] , Chang-Hua Qiu[1] and Manuchehr Soleimani[2]

1. Industrial Tomography Systems Plc, Manchester, U.K.

2. Engineering Tomography Laboratory (ETL), Department of Electronics and Electrical Engineering, University of Bath, U.K.

Abstract

Electrical Capacitance Tomography (ECT) is a non-invasive imaging technique that is sensitive to dielectric permittivity property of an object. The conventional ECT system are in circular/cylindrical geometry, where the electrode plates are usually located equally around the circular tank. It is the most common configuration as it can be easily applied to industrial pipelines. However, under some circumstances, the circular geometry may not be applicable due to the limitation of the process area. For example, there are several industries that implement rectangular vessels instead of circular vessels. In those cases, and with limited access, planar ECT sensors can fit the process structure better and hence can obtain a more accurate information. Single-plane ECT configuration have been proposed for such applications. However it often suffers from small sensitivity depth. To overcome this problem, we explore further of the planar ECT geometry; from the single-plane ECT to dual-plane ECT structure. The limitation and the constraints of planar configuration will also be discussed. Several experiments were conducted using both single-plane and dual-plane configurations to evaluate the potential applications. The initial results are promising, and the quality of the reconstructed images will be compared with the real condition for process validation.

Keywords: Electrical capacitance tomography, planar array, single-plane ECT, dual-plane ECT

1 Introduction

Electrical Capacitance Tomography (ECT) is a type of imaging technique which has been developed for industrial processes [1]. ECT is sensitive to dielectric materials, for example, polymer, oil, composite materials and water. These materials are involved heavily in many industries [2], therefore ECT has been a very attractive imaging technique since it was first invented [3, 4]. Usually, an ECT sensor has an array of electrode plates that are attached circumferentially around the process vessel. By systematically applying a potential to one of the electrodes (excitation electrode) and measure the capacitance between the excitation electrode and the rest of the electrodes, a distribution of the changes of permittivity map can be produced that provide essential information about the industrial processes.

When a typical ECT system is designed, its electrode plates array are normally arranged around the target object (pipes, vessels or tanks), assuming there is free access around the complete process area. However, this assumption is not always valid. In many industrial processes, the process pipe/vessels are in rectangular shape instead of circular shape, secondly, the access of the vessels' peripheral is not always available. In this case when there is limited access to the process region under testing, the traditional circumferential ECT cannot be applied. This is the reason why there has been growing interest in planar array ECT [5, 6, 7, 8, 9]. This paper aims to investigate a configuration that can overcome the challenges described above. In order to obtain the process information from a rectangular pipe/vessel, with a limited access of its circumference. There have been several studies that propose the signal-planar configuration, however, its biggest disadvantage for single-plane ECT is its shallow sensitivity depth [5]. Having one extra plane in the system, the sensitivity depth can be improved significantly, hence a complete process condition within the rectangular vessel can be visualised and a more accurate result can be obtained. Here, a dual-plane ECT model is developed for 3D ECT visualisation, as there are more works are done recently on 3D electrical capacitance tomography [10, 11, 7]. In this paper, a complete analysis on the dual-plane ECT geometry will be investigated. Results and discussion of the influence of one extra plane will also be discussed. The paper verifies this dual-plane ECT using experimental data, which in turns validate the potential of this configuration to be applied into real industrial applications.

2 Planar ECT System Setup

In this paper, a commercialised ECT instrumentation system was used for data acquisition for all the experiments in this paper: M3C ECT system from Industrial Tomography Systems Plc. (ITS). The M3C instrument can support up to 24 channels ECT sensor, with an accuracy of 0.01 pF (Figure 1 (a)). Therefore it is suitable for either 12 or 24 channel ECT sensors, which are the most common channel numbers for commercialised ECT systems. The planar

(a)

(b)

Figure 1: (a) ITS 24 channel ECT M3C system and (b) the developed PCB 3×4 electrode array

ECT sensors were designed accordingly using double sided printed circuit boards (PCB). The overall dimension of the PCB sensor is 13.5 cm x 13.5 x 0.15 cm, and the electrode area (sensing region) is 11.0 cm x 11.0 cm, as shown in Figure 1 (b). On the top layer of each sensor, 12 electrodes are arranged in the 3 x 4 grid pattern. The dimension of each electrode is 2.5 cm x 3.5 cm. A grounding conductor is surrounding the electrode array to act as a guarding electrode. The bottom layer of the PCB is pure copper plate, acting as an external shield of the planar sensor. This extra copper layer can protect the capacitance sensor from the external interferences.

To conduct dual-plane experiments, the location of both PCB boards need to be positioned co-axially, i.e. the location of the opposite electrodes need to have the same y and z position. If the planar sensors are mis-located, there will be some mismatch between the system model and the real condition, hence the reconstructed image will not be accurate. For the planar separation analysis

(Section 2.1), a 1.0 cm grid reference sheet was used to correctly determine the separation distance. Each sensor plate was supported with a plastic stand to ensure that the planar sensors are positioned in up-right positions. The plastic stands also help the sensor alignment, which can minimise the distance error (Figure 2).

Figure 2: The experimental system setup for the dual-plane ECT configuration.

2.1 Plane Separation Analysis

For single-plane ECT geometry, the sensitivity region tends to have a trapezoidal or semi-spherical shape, as shown in the gray region of Figure 3. The measurement from the furtherest electrode pair (electrode 1 and 12 for instance) contribute to most of the significant depth, nevertheless it also has the poorest signal to noise ratio (SNR) [7]. This phenomenon causes the 'blind spot' effect when the single-plane ECT is used for process detection in a rectangular pipe. This is the major drawback for single-plane ECT configuration, i.e. the measuring object becomes undetectable if the measuring object is further away from the planar sensor. In [7], it claims that a maximum depth of 53 % of the ECT sensor array length can be achieved, however it is only achievable if the measuring object is located at the centre location of the plane, which has the deepest sensitivity region. For industrial applications, this feature can cause inaccurate process measurement, as the sensitivity region might not cover the entire process region (see Figure 3 (a)).

The proposed dual-plane configuration can overcome such problem (see Figure 3 (b)). By having one extra opposite plane, the SNR degrading problem can be compensated when the object is moved away from one of the sensor plates.

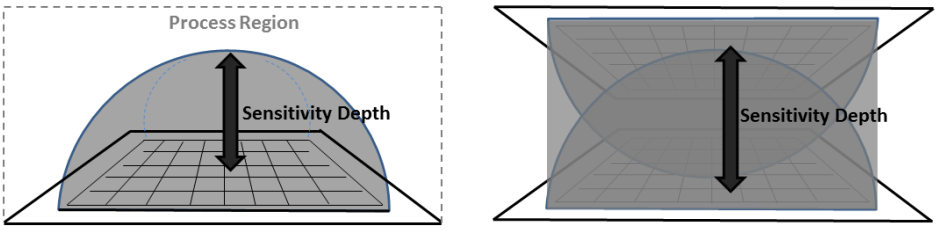

(a) (b)

Figure 3: The sensitivity region of a (a) single ECT planar sensor and (b) dual ECT planar sensor.

In our planar ECT system, ITS M3C instrument is used to acquire capacitance signal. Due to the existence of stray capacitance, the ECT measurement is always the sum of the induced voltage and the stray voltage. The induced voltage is the signal induced from the excitation electrode, and the amplitude of the signal is a function of the permittivity distribution and the separation distance between the excitation electrode and the receiving electrode. The stray voltage is the signal caused by the stray capacitance (from the data acquisition systems and cables). This stray signal is not correlated with permittivity distribution; hence the signal does not contribute much to the image reconstruction. A proper separation distance needs to be selected to ensure that the measurements from the ECT electrode are dominated by the induced voltage, but not the stray voltage. In this case, the overall sensitivity can be enhanced and the blind spot within the rectangular process region can be minimised.

An experiment was conducted to find the appropriate separation for the dual-plane ECT geometry. In the experiment, the distance between the sensor plates was 2.0 cm initially. Electrode 1 was excited with an 18V p-p, 1 MHz sinusoidal signal, and the capacitance signals from electrode 13-24 were measured (see Figure 1(b) for electrode position). The same procedure was repeated with 4.0, 6.0, 8.0, 10.0, 12.0, 14.0 and 16.0 cm separation. Two hundred samples were taken at each separation distance, and the time gap between each frame is set to 1 second, to ensure the sample independency.

From the capacitance theory, it is expected that the voltage signal shall decrease when the separation distance becomes greater, i.e. poorer inter-plate coupling. Figure 4 shows the raw voltage signals for the opposite electrode pairs measurements, i.e. the voltage measurements obtained from measuring electrode 13, 14, 17 and 18, when electrode 1 is driven by a sinusoidal signal. These neighboring opposite electrode pairs are selected because they tends to have the largest signal strength which contribute the most towards the image reconstruction.

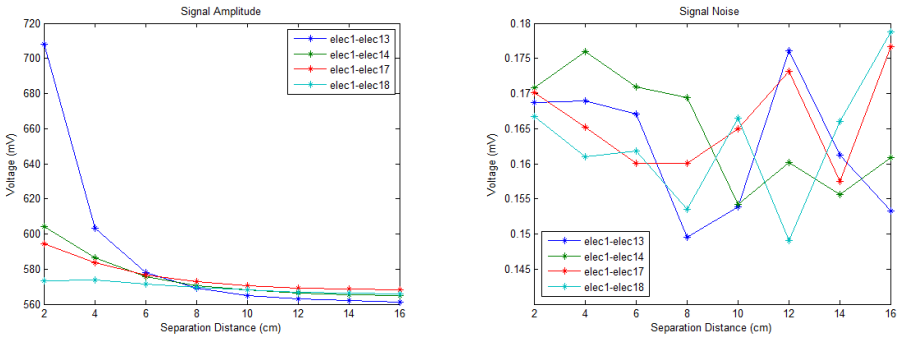

(a) (b)

Figure 4: The ECT (a) signal and (b) noise level at different electrode pairs with different separation distances.

From Figure 4, a sharp decrease of signal strength is observed when the separation distance increase from 2cm to 8cm; meaning that under this distance range, the measurement signal contains induced voltage, which can reflect the change of the permittivity distribution. When the ECT sensor planes are separated by more than 10cm, the signal measured on the electrode plates are mainly the stray signal, hence the signal strengths remain almost constant regardless of the increasing distance.

The noise signal was also calculated based on 200 samples at each separation. It is observed that the signal noise level varies randomly from 0.15mV to 0.18mV. The correlation between the signal noise and the separation distance are calculated; the correlation factors for electrode combination 1-13, 1-14, 1-17 and 1-18 are 0.3584, 0.7930, 0.2166 and 0.2708 respectively. This indicates that the sensing noise is poorly correlated with the separation distance. SNR values can be calculated from the signal and noise plots in Figure 4. For electrode combination 1-13 for instance, SNR of 71.5dB can be achieved when the separation is 4.0 cm.

Another sensitivity test was setup to further validate the optimal plane separation (see Figure 5(a)). A 1.5 cm diameter cylindrical plastic rod was inserted in between two ECT planes with an initial separation of 4.0 cm. With a good separation distance, the insertion of the plastic rod should produce enough contrast on measurement signals, in order to reconstruct a satisfactory tomogram. If the measurement signal remain unchanged when the inclusion is inserted, it means that the separation distance is too far and there is no coupling between the ECT sensor plates. The signal contrast was measured repeatedly when the separation distance was increased to 6.0 cm, 8.0 cm, 10.0 cm, 12.0 cm, 14.0 cm and 16.0 cm. In this test, we used a rule of thumb assuming that the signal perturbation must be 2 times larger than the noise level to reconstruct images successfully. Figure 5(b) shows the number of electrode pair measurements (out of 276) that have voltage changes which are two times larger than the noise

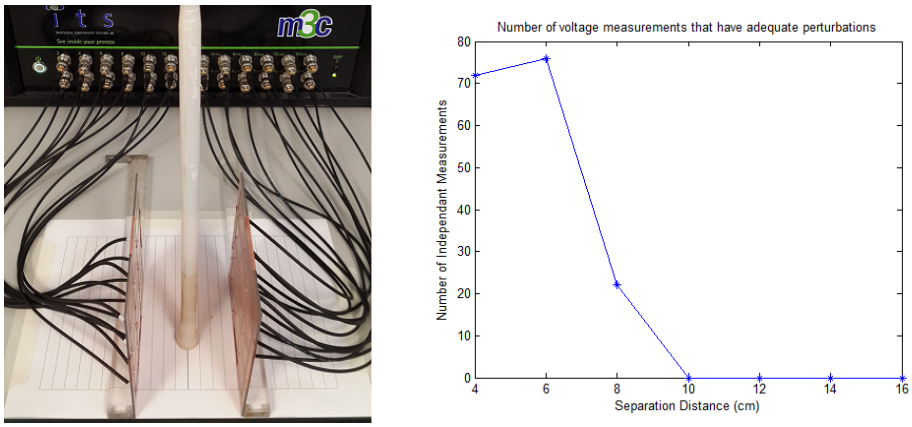

(a) (b)

Figure 5: (a) The sensitivity test setup at 8.0 cm separation and (b) Signal perturbation analysis with different separation distance.

level, when the plastic rod is placed in between the ECT planar sensors.

From both the signal to noise analysis and the sensitivity analysis, a separation of 4.0 to 6.0 cm is found to be the most suitable separation range for the 11.0 cm×11.0 cm dual-plane ECT configuration. Figure 5(b) indicates that when the distance is greater than 8.0 cm, the perturbation caused by the inserted plastic rod is too small and most of the voltage changes in the measurements can easily be buried within the system noise. In this situation, there is weak coupling between two ECT sensor plates and the dual-plane configuration will behave like two single-plane ECT sensors, i.e. the opposite planes are not communicating with each other. This statement can be demonstrated by the following tests shown in Figure 6.

The figure shows the signal contrast between two scenarios: a wooden board inclusion measured using a single-plane sensor (66 electrode pair measurements), and the same wooden board measurement using a dual-plane sensor with 10.0 cm separation (276 electrode pair measurements) . The wooden board inclusion has a dimension of 27 cm×8 cm×1.5 cm and is placed at the same location for both single plane and dual plane tests. Both the measurements are referenced against the empty sensor measurement. In the figure, the 66 single plane signal contrast is shifted to the right for the ease of comparison. From the overlapping region, one can see that the information provided by both tests is almost identical. When the separation distance is too large, adding an extra planar sensor does not add value to the measurement. Although for the dual-plane signal, there are 210 more measurement values than the single-plane signal, those extra measurements are below noise level (average contrast = 0.23mV) and do not contribute towards the image reconstruction. Similar tomography results

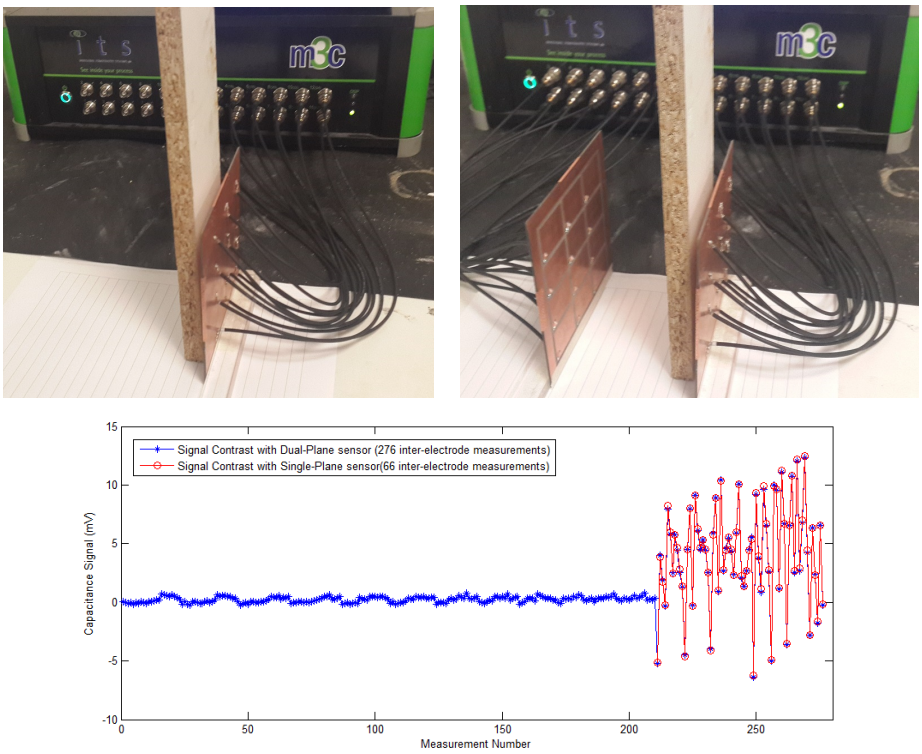

Figure 6: The signal contrast comparison when a wooden board inclusion is inserted into a single-plane sensor (red 'o' plot) and a dual-plane sensor (blue '*' plot).

are expected as those small capacitance contrasts in the dual-plane case will be covered by inversion regularisation.

From the separation analysis results, a separation distance of 4.0 cm is applied for all our dual-plane experiments conducted in this paper, in order to achieve the best performance.

3 Image Reconstruction

The aim of the electrical tomography is to obtain the process information from the reconstructed image. Therefore selecting a good image reconstruction method is vital if ECT is used as a process monitoring tool. The image reconstruction process can be divided into two parts: forward problems and inverse problems.

3.1 Forward Modeling

Before reconstructing an ECT image, a computation model for the planar configuration is required. This computational modelling is called forward problem. In ECT, the forward problem is the simulation process of calculating the electric potential distribution based on the given sensor configuration, system geometry and the excitation patterns. In order to simulate an accurate model, the system geometry and excitation patterns must be in consistent with the real situation. For ITS M3C system, an 18V p-p 1 MHz sinusoidal voltage is excited to an electrode, and the electric charge is then measured on each of the remaining electrode. Each electrode will take turns becoming the excitation electrode in the consequence cycles. For this reason, the number of measurements in a typical ECT system is corresponding with the total number of electrodes: $M = N(N-1)/2$, where M is the number of independent measurements and N is the number of ECT electrode in the system. The forward problem of ECT is mainly solved by the Maxwell's equation. Since ECT is considered as a near field model, it is assumed that the internal charges and the wave propagation effect are negligible. Hence the electrostatic approximation $\bigtriangledown \times E = 0$ can be defined. The relationship between the permittivity distribution and the boundary electrical potential are given by the Poisson's equation

$$\nabla \cdot (\varepsilon \nabla u) = 0 \tag{1}$$

where ε is the dielectric permittivity and u is the electric potential. And the boundary condition are the following:

$$u(x) = V \quad on\, \tau_{excitation} \tag{2}$$

$$u(x) = 0 \quad on\, \tau_{others} \tag{3}$$

where V is the excitation voltage, $\tau_{excitation}$is the surface where the excitation electrode is, τ_{others} is the surface of all other sensing electrode, including grounding plate. Once these parameters are all defined, the electric charge on the electrode k can be expressed using Gauss's law:

$$Q_k = \int_{\tau k} \varepsilon(x) \frac{\partial u(x)}{\partial n} \delta\tau \tag{4}$$

where n is the inward normal on the electrode surface k. Finite element method (FEM) is normally used to solve this equation.

Since the relationship between the measured voltage and the permittivity of each voxel is non-linear, a Jacobian matrix is required to linearised the relationship. The sensitivity map can be calculated based on the calculated field distribution from Equation 4. The formulation of ECT forward modelling and

sensitivity map calculation are also discussed in [12, 13, 14, 10], the generalized equation is

$$\frac{\partial C_{ij}}{\partial \varepsilon} = -\int_{\Omega} E_i \cdot E_j \delta\Omega \tag{5}$$

where the right hand side is the volume integral of $E_i$and E_j, the electric field distribution over the entire sensing region Ω when electrode i and j are the excitation electrodes respectively. The output of the equation $\frac{\partial C_{ij}}{\partial \varepsilon}$ is called the Jacobian matrix. Each row of the Jacobian matrix represents the sensitivity of one electrode pair measurement data with respect to all the voxels. The Jacobian matrix is therefore a matrix that contains the relationship between capacitance and the permittivity for all possible combination of electrode pairs. Each element within the Jacobian matrix indicates the change of the capacitance between a particular electrode pair due to the permittivity change in particular voxels within the perturbation region. Figure 7 shows the FEM model generated by COMSOL and the computed sensitivity map with different electrode pairs using MATLAB. The models are all developed based on the real geometry.

3.2 Inverse Problem

For 2D ECT, Tikhonov based method is commonly used for solving inverse problem to improve the ill-posed issues [15, 16]. However this might not be suitable for 3D reconstruction due to the large number of mesh elements. For a calculated sensitivity map $J \in \mathbb{R}^{m \times n}$, where m is the number of independent measurement of the system, and n is the total number of FEM voxels. When there are many mesh elements, $J^\top J$ multiplication will require a huge memory resource, which make the standard Tikhonov method unsuitable for real time reconstruction. To avoid the $J^\top J$ calculation, a Wiener filter is applied to the standard equation, which can overcome the limited computational resource issue. The principle of this alternative solver is discussed in [16]. Equation 6 shows the Tikhonov inverse solver in Wiener filter form:

$$x = J^\top (JJ^\top + \lambda R)^{-1} b \tag{6}$$

, where J is the sensitivity derived from Equation 5, b is the sensor measurements, x is the reconstructed images, λ is the regularisation parameter and R is the regularisation matrix. R is generally an identity matrix, assuming that all the voxels are independent with each other. In Equation 6, one can notice that the $J^\top J$ multiplication is replaced by $JJ^\top$, which consumes a much smaller computational resource.

To ease the image visualisation and post-processing, all the reconstructed images are normalised against a high permittivity reference signal (when the sensor is filled with polyethylene beads). After the normalisation, ideally, all

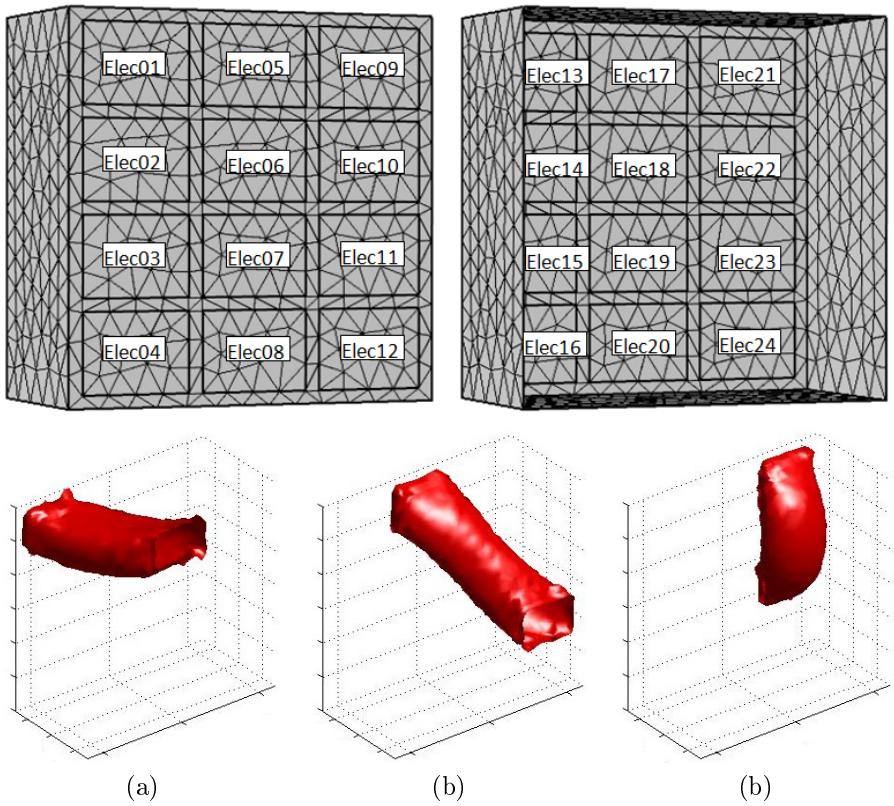

Figure 7: The FEM mesh model and the computed sensitivity map between (a) electrodes 01&13, (b) electrodes 11&17, and (c) electrodes 21&23

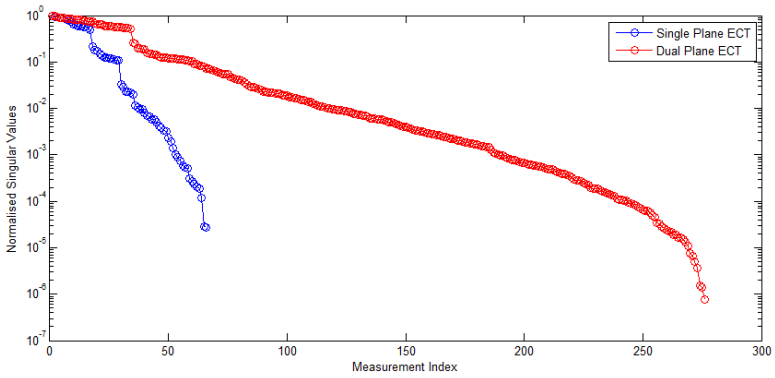

Figure 8: Singular value plot for single-plane ECT and dual-plane ECT.

the voxels in the reconstructed tomogram shall have values of 0 when the sensing region is empty. And when the sensing region is filled with polymer beads, all the voxels values will have values of 1.

3.2.1 Singular Value Decomposition Analysis

The singular value decomposition (SVD) is an useful tool for analysing problems with ill-posed matrices, as the truncated SVD method has been used for solving a variety of discrete ill-posed problems successfully. Singular value decomposition of the Jacobian matrix provides an important information to analyse the behaviour of the underlying inverse problem. Hence, in order to determine how image quality improves for the dual-plane configuration, a singular value decomposition graph is computed. Figure 8 shows the SVD decay plot to determine the level of ill-posedness for single plane ECT and dual-plane ECT respectively.

From Figure 8, it can be seen that the plot for single plane ECT has a sharper decay rate, which indicates that it is more ill-posed than the dual plane ECT. To resolve ill-posed problems, ECT reconstruction requires regularisation, and different level of ill-posedness will respond differently to the regularisation. In this paper, the authors utilise the 'resolution operator' method, image quantification and visual inspection to find the optimal regularisation parameter.

3.2.2 Resolution Analysis

In Equation 6, there is a parameter λ that determine the level of regularisation in the inverse solver. The reliability of the reconstructed permittivity distribution depends heavily on the selection of parameter λ [17]. In order to select an appropriate regularisation parameter for the inverse solver, the resolution

matrix, a tool which can identify the reliability of the inversion, is used in this paper. The resolution matrix method has been previously implemented mainly in the inverse theories in geophysics field [18].

Taking the equation $b = Jx_{true}$, and substitute it into the inversion equation 6:

$$x_{model} = J^{\top}(JJ^{\top} + \lambda R)^{-1} J x_{true} \tag{7}$$

The resolution matrix can then be defined as

$$Res = J^{\top}(JJ^{\top} + \lambda R)^{-1} J \tag{8}$$

From Equation 7, the x_{model} should be equal to x_{true}in the ideal scenario, i.e. Res will be an identity matrix. The diagonal elements of resolution matrix are a strong indication of uniformity of reconstruction process. In real situation, the closer the resolution matrix Res is to the identity matrix, the better inversion reliability is achieved. In this paper, the permittivity distribution $x_{reconstruction}$ is modeled by using 16384 voxels. In the ideal case, the resolution matrix Res shall be an identity matrix of 16384×16384, and the sum of the diagonal values should be 16384. Because of the ill-posed nature of ECT inverse problem, in the 3D reconstruction the sum of the diagonal values of Res will be significant smaller than the ideal value 16384. By selecting a regularisation parameter λ that can provide the highest sum of the diag(Res), the better sensitivity uniformity can be achieved. One of the major issues for planar ECT is its strong non-uniformity in sensitivity, so the authors choose the uniformity as a measure for selecting the regularisation parameter. Figure 9 shows the sum of diag(Res) with respect to a wide range of regularisation parameters for single and dual plane geometry. Based on the resolution matrix curve, the ideal regularisation parameter can then be selected. From the Figure 9, it is shown that under the dual plane configuration, the inversion is most reliable when $\lambda = 8e11$.

It is worth noting that the resolution matrix curves for single-plane and dual-plane behave differently. For example, the sum of the diag(Res) for dual-plane configuration is higher than the summation of the single-plane configuration, which indicates that dual-plane ECT has a better sensitivity uniformity. This may be due to the different levels of ill-posedness, as from the SVD analysis, dual-plane ECT has a less ill-posed nature (slower singular value decay rate).

3.2.3 Regularisation vs Accuracy

After finding an appropriate reglarisation parameter using resolution matrix, a simple test was conducted to find the optimal parameter, in a more objective manner. In the experiment, a rod with a 2.0 cm×2.0 cm cross section area is inserted in the dual-plane ECT sensors with 4.0 cm separation, as shown in the

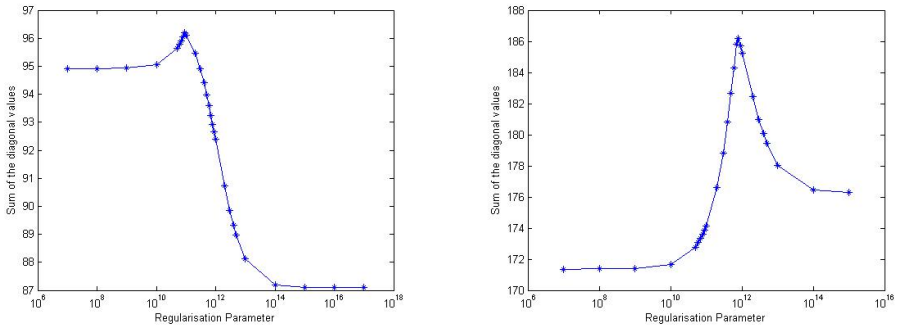

(a) (b)

Figure 9: The sum of the resolution matrix's diagonal values with respect to a range of regularisation parameters for (a) single-plane configuration and (b) dual-plane configuration.

Figure 10. The same acquired data is used to reconstruct the tomograms using 5 different regularisation parameters near the value 8e11, which supposes to be the regularisation with the most uniform sensitivity. Then, the optimal regularisation value can be selected based on visual inspection and image quantification. The relative error (RE) parameter is used for quantifying image quality, RE can be calculated by the following equation.

$$RE = \frac{\|\varepsilon_{calc} - \varepsilon_{true}\|_2}{\|\varepsilon_{true}\|_2} \tag{9}$$

, where ε_{calc} is the reconstructed permittivity pixel values, and ε_{true} is the pixels distribution based on the true condition. Figure 10 shows the image reconstruction results using different regularisation values and their corresponding RE values.

From the visual inspection, λ values with 5e11 and 8e11 produce the best rod shape reconstruction. When the λ is deviated from the 8e11 value, image artifact starts appearing in the image. And also from the RE analysis, λ values with 5e11 and 8e11 give the least relative error, larger RE value for 8e11 λ value indicates that the reconstructed image is a bit over-regularised. By considering both relative error and visual inspection, the regularisation value of 5e11 are selected for all the image reconstruction for dual-plane ECT configurations. The same test was performed for the single plane ECT and the regularisation parameter of 8e10 is chosen for all the single-plane reconstructions in this paper.

$\lambda = 5e10$	$\lambda = 1e11$	$\lambda = 5e11$	$\lambda = 8e11.$	$\lambda = 5e12$
RE = 0.7457	RE = 0.6998	RE = 0.5750	RE = 0.5805	RE = 0.6707

Figure 10: Image reconstruction result with different regularisation values.

4 Experimental Setup and Results

Several ECT experiments were carried out using the planar configuration. As mentioned in Section 2, both the PCB sensor array has an electrode area of 11 cm ×11 cm, and the distance between two boards is 4.0 cm for the best performance. Figure 11 shows the complete experimental setup for the dual-plane configuration. The experiments are divided into two categories: isolated object detection and the interface detection.

4.1 Isolated Object Detection

The aim of this experiment is to demonstrate the dual-plane sensor has the capability to determine the shape and the location of the inclusion objects. The initial experiments were conducted using single-plane configuration (see Figure 12), to demonstrate the sensitivity depth problem discussed in Section 2.1. In Figure 13, a plastic rod is positioned with vertical and diagonal directions, in various locations inside the dual-plane ECT sensor. And for the last isolated test, an empty plastic tube is covered up with polyethylene beads, to simulate an air bubble in a process oil. All the reconstruction processes are using the inverse algorithm described in Section 3.2. In each reconstructed tomogram, there are 16384 voxel values to represent the 4 cm×11 cm×11 cm volume. Selecting an appropriate method to visualise all the 16384 voxels is important for

Figure 11: The system setup for the dual-plane ECT configuration.

understanding and analysing the process. For this object inclusion experiments where the inclusion is an isolated sample, the 3D contour 'iso-surface' method is a better visualisation method to show the shape and the position of the inclusion. And since the reconstruction result is normalised between 0 and 1, the contour level selection process can be simplified. In this paper, a contour level of 0.5 is selected for all our ECT reconstruction. Changing the contour level can alter the visualisation outcome, however it is believed that using a contour level of 0.5 can provide the most unbiased result.

4.2 Interface Detection

For some industrial applications, interface (and level) detection is an important tool for process monitoring. For example, liquid-foam interface detection is often required in food/drink industries as bubbles can be naturally produced during the manufacturing process. Oil and gas interface detection is also commonly found in petrochemical industries, to determine the concentration of oil and gas in the production fluids. Since ECT sensors are sensitive to dielectric materials, it can certainly be used in monitoring the process that involves with both oil ($\varepsilon_r \approx 3$) and gas ($\varepsilon_r = 1$). In this experiment, the feasibility of using ECT

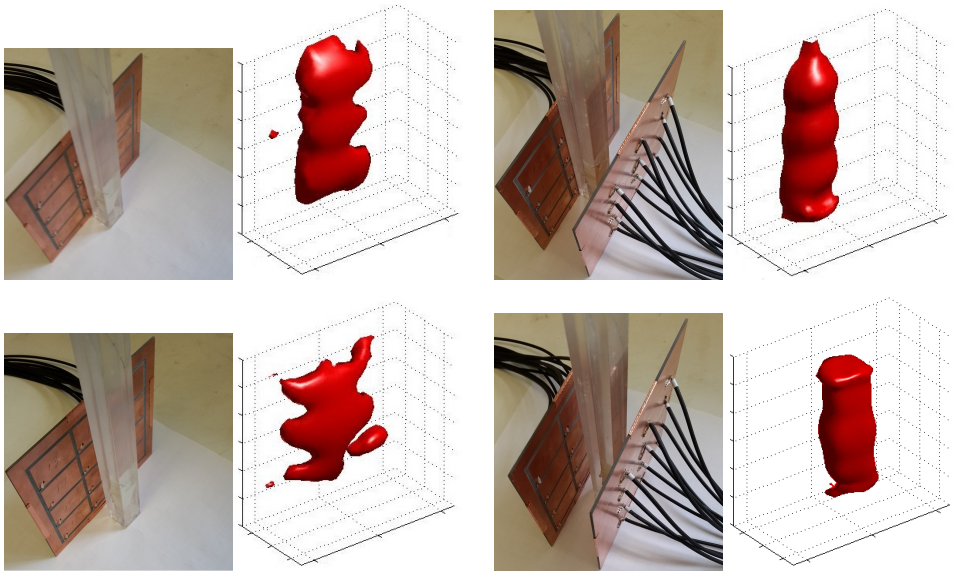

(a) (b)

Figure 12: Image reconstruction comparison between the (a) single-plane and (b) dual-plane configuration. The separation distance between the planar array and the plastic rod is 0 cm and 2 cm for the top images and bottom images respectively.

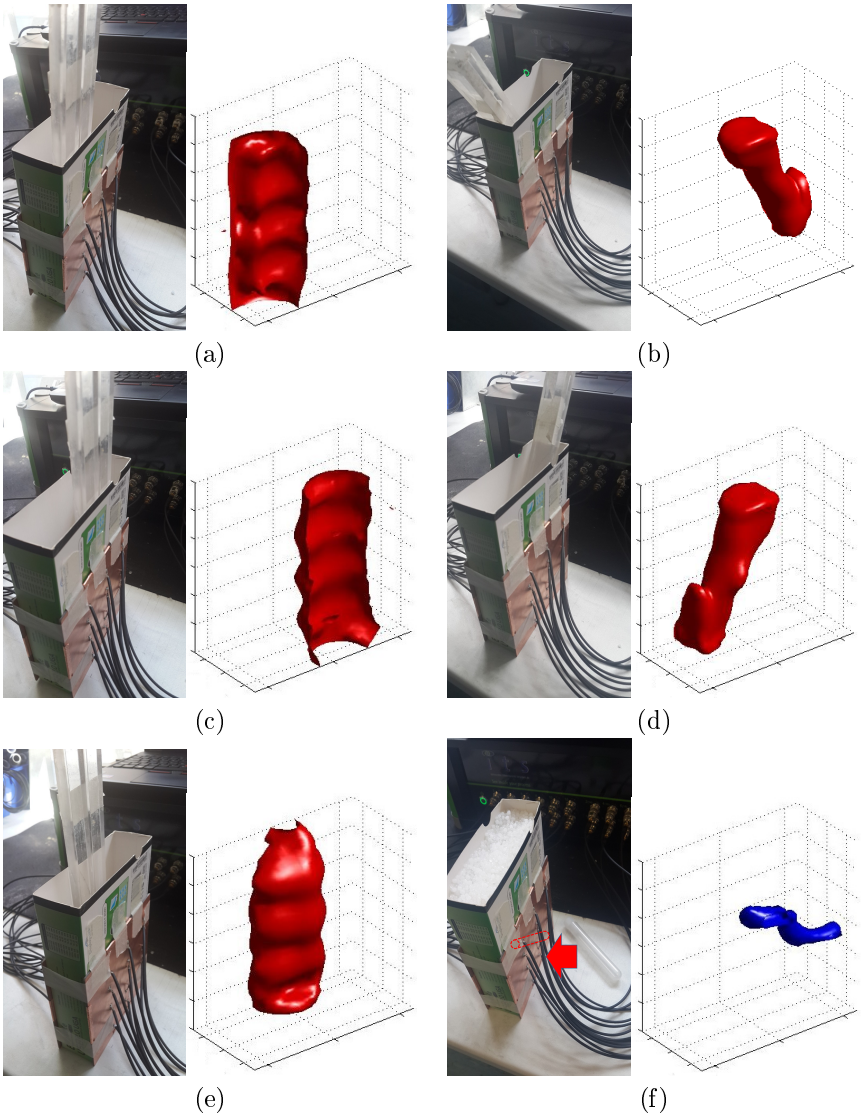

Figure 13: Reconstructed results of the isolated object experiments. (a - e): Images of a moving plastic rod in various locations within an empty dual-plane ECT sensor. (f): The image of an empty plastic tube buried in polyethylene beads, to simulate an air bubble in process fluid.

as a oil/gas interface detector is demonstrated. Polyethylene beads are used to simulate the process oil, as they have similar relative permittivity values. Different amount of the polyethylene beads are added into the sensor region in steps to create different oil and gas ratio. The signals are acquired by the ITS M3C system and the 3D images are then reconstructed. Figure 14 shows the imaging results of the oil and gas ratios are 0:5 (0%), 1:4 (20%), 2:3 (40%), 3:2(60%), 4:1 (80%) and 5:0 (100%) respectively. Slice visualisation method is used in this example. Although the slice visualisation only provide a cross section of the tomogram and does not reflect the entire volumetric region, it produces better visualisation effect for this interface detection application.

To validate the accuracy of the image reconstruction process, the reconstructed images need to be converted to a useful analytical data. In this case, since the 3D images are normalised, the tomograms can easily be post-processed by averaging all the voxel values to quantify the level information. The interface levels are calculated by summing all the voxels which have values greater than the contour level (0.5 in this case), then divided by the total voxel numbers. The interface level formula is equated as follows:

$$InterfaceLevel = \frac{1}{n}\sum_{k=i}^{n} x_k[x_k > 0.5] \tag{10}$$

where n is the total number of voxels in the image, k is the voxel index, and $[x_k > 0.5]$ is the Iverson bracket which gives the condition for summing only the voxels that have values greater than the contour level. This equation was originally used for void fraction calculation. Since in this experiment, the level varies in axial direction only, i.e. the interface is always a flat surface, the void fraction equation is also valid for interface level calculations. Nevertheless for more complicated scenarios, different equations (combined with 3D tomograms) will be required to extract the interface profile, which is beyond the scope of our paper. Figure 15 shows the quantified results for the experiment. To further demonstrate the advantage of dual-plane configuration over the single-plane configuration, the same experiment was repeated using a single-plane ECT configuration.The interface level result are then compared and analysed based on the accuracy and the image stability.

5 Discussion

In this paper, both single-plane and dual-plane ECT configuration systems are evaluated using the experimental data. From the isolated object detection experiment result (Figure 12), it can be seen that when the isolated object is

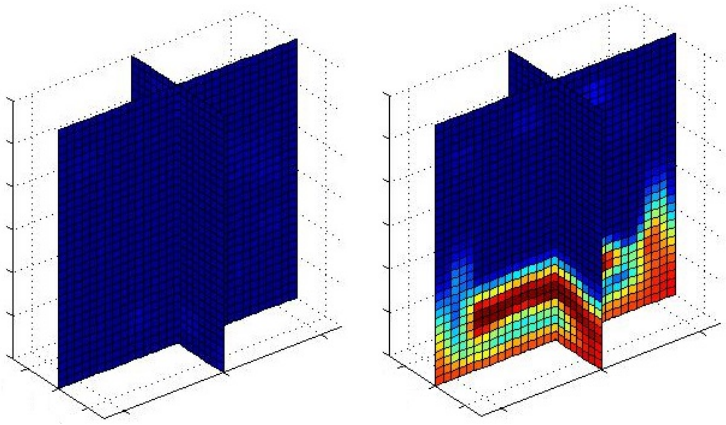

(0% Polyethylene level)

(20% Polyethylene level)

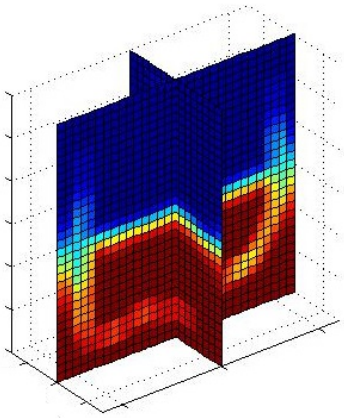

(40% Polyethylene level)

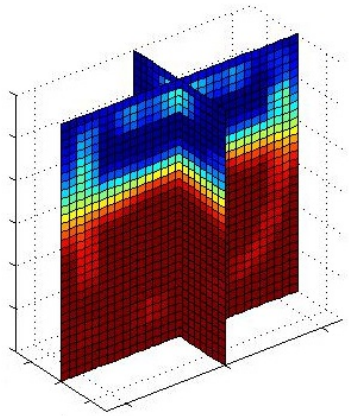

(60% Polyethylene level)

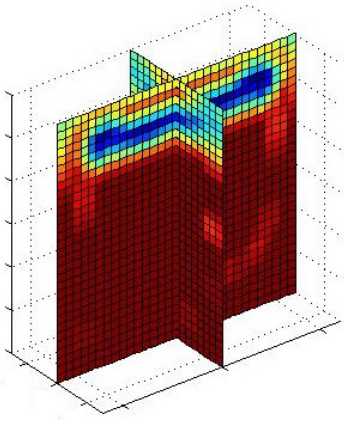

(80% Polyethylene level)

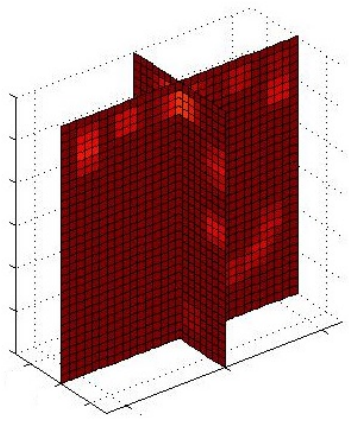

(100% Polyethylene level)

Figure 14: The reconstructed images of various polyethylene levels in the dual-plane sensor.

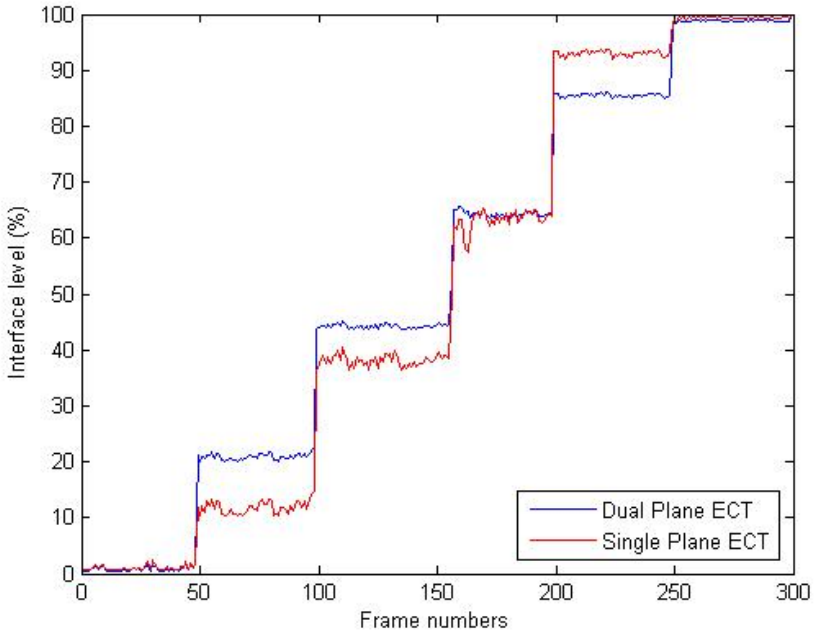

True Level (%)	Computed Level (Dual-Plane)	Computed Level (Single-Plane)
0%	0.81±0.43 %	1.05±0.49%
20%	20.90±0.52%	11.78±1.05%
40%	44.22±0.37%	38.13±1.00%
60%	64.37±0.48%	63.32±1.72%
80%	85.51±0.29%	93.03±0.48%
100%	98.80±0.15%	99.33±0.19%

Figure 15: The reconstruction accuracy comparison using the dual-plane and single-plane ECT configuration.

moved away from the single-plane sensor, the reconstructed object will be distorted and cannot provide reliable information about the measuring object and the distance. However using the dual-plane configuration can resolve the issue. More experiments were conducted using dual-plane configuration. In Figure 13, it shows that the dual-plane ECT can correctly determine the location, shape and size of the inclusion object. The air bubble simulation experiment further strengthen the fact that the planar configuration can be applied into the real industrial application, provided that the process vessel is in the rectangular shape. The dual-plane ECT study is then further extended for the industrial interface detection applications. From Figure 14, the slice tomograms correctly determine the amount of polyethylene beads added inside the sensing region. Again, to demonstrate the advantage of the dual-plane over the single-plane configuration, the same experiment is also repeated with a single plane sensor. Figure 15 shows the image quantification result, and it can be clearly seen that the dual-plane configuration can obtain a more accurate interface estimation (less than 5 % error) than the single-plane configuration. It is also observed that under the 40% and 60% filling level, the dual and single planes produce similar estimations, this is because the single plane configuration has a better sensitivity in the central region (see Figure 3). However, when the interface level is not within the central region, dual plane configuration is required in order to enhance the sensitivity uniformity in the other region.

The dual-plane configuration is proposed to overcome the small sensitivity depth problem of the single-plane configuration. Although there has been studies stating that a maximum of 50 % of the electrode array length penetration can be achieved. It is shown in the experiments that the reconstructed image does not reveal the true condition accurately enough, even the depth of the processing region is only 4.0 cm /11.0 cm = 36% of the sensor array length. Using the dual-plane configuration can improve this issue. The suitable plane separation distance for dual-plane configuration is characterised. In this paper, the separation distance of the planar sensor is chosen to be 4.0 cm for all the experiments. This distance can be increased to $\approx$6.0 cm according to the analysis in Figure 4 and Figure 5. However, the longer the sensor planes are separated, the less the sensor planes are coupled together, hence the sensitivity will be degraded and the reconstruction accuracy will be affected.

Increasing the electrode array size can effectively increase the sensitivity depth. With a sensitivity depth limit of 6/11$\approx$55% sensor side length limit, it will certainly bring impacts towards the applicability of the planar ECT configurations. However, there are still many industrial processes that can utilise this planar setup effectively, for example the processes that involve rectangular pipe for gas/oil distribution. For any rectangular pipe that has width: height ratio from 1:0.2 to 1: 0.6, the planar ECT sensor can be attached externally onto the opposite sides of the pipe to monitor the flow regime.

6 Conclusion

This study represents the proof of principle for dual-plane ECT as an useful tool for visualising 3D industrial processes. The experimental results are promising, the reconstructed 3D tomograms indicates that the dual-plane ECT can potentially be a good interface detector, for the oil/gas industries. Using the uniformity as a measure for selecting the regularisation parameter is also proposed in this paper, as the strong non-uniformity in sensitivity is one of the major issues of the planar ECT. Based on our knowledge this has not been proposed before, but our experimental evaluation in this study shows that acceptable images can be reconstructed by selecting a regularisation with the highest uniformity for the planar models. Although the resolution matrix plot does not contradict the findings from the SVD analysis, it will be interesting to see in more rigorous mathematical studies how this measure of uniformity act as a stabiliser for the image reconstruction process, something that is beyond scope of this work.

One drawback of the dual-plane configuration is the data acquisition time. By increasing the number of electrode from 12 to 24 in the system, the number of independent measurement in each sample will be increased from 66 to 276, which means that the system frame rate will be slow down by more than 4 times. To apply such configuration, a high speed ECT instrument is required.

More evaluations can be carried out in future studies, for example using different planar configurations (perpendicular setup instead of parallel setup) for other types of industrial applications. Furthermore, a linear ECT configuration can also be improved from this planar ECT research outcomes, as they share many design aspects with each other. Linear probe is an attractive configuration as it can inserted into a vessel to monitor viscous or non-Newtonian fluid processes, but it also suffers from the same problem of small sensitivity penetration. Using the dual-plane configuration can enhance the sensitivity between sensor planes and potentially overcome the issue. To adapt the dual-plane configuration, the sensor need to accommodate to the vessel size. Due to the restriction of the separation distance, the electrode size and driving signal have to be adjusted to enhance the sensitivity to cover the entire vessel. However this is out of the scope of this paper and will be the subjects of our follow up studies.

7 Acknowledgments

The authors would like to thank the UK Technology Strategy Board (TSB) for support of this work on the Knowledge Transfer Partnership (KTP) project (KTP009034).

References

[1] W. Q. Yang, "Design of electrical capacitance tomography sensors," *Meas. Sci. Technol.*, vol. 21, p. 042001, 2010.

[2] C. Ortiz-Aleman and R. Martin, "Electrical capacitance tomography two-phase oil-gas pipe flow imaging by the linear back-projection algorithm," *Journal of Geophysics and Engineering*, vol. 2, pp. 32–37, 2005.

[3] G. E. Fasching and N. S. Smith, "A capacitive system for 3-dimensional imaging of fluidized-beds," *Rev. Sci. Instrum.*, vol. 62, pp. 2243–51, 1991.

[4] J. S. Halow, G. E. Fasching, P. Nicoletti, and J. L. Spenick, "Observations of a fluidized-bed using capacitive imaging," *Chem. Eng.Sci.*, vol. 48, pp. 643–59, 1993.

[5] X. H. Hu and W. Q. Yang, "Planar capacitive sensor: designs and applications," *Sensor Review*, vol. 30 (1), pp. 24–39, 2010.

[6] D. X. Chen, X. H. Hu, and W. Q. Yang, "Design of a security screening system with a planar single-electrode capacitance sensor matrix," *Meas. Sci. and Technol.*, vol. 22 (11), p. 114026, 2011.

[7] Z. Ye, R. Banasiak, and M. Soleimani, "Planar array 3d electrical capacitive tomography," *Insight*, vol. 55 (12), pp. 675–680, 2013.

[8] F. Wang, Q. Marashdeh, L. Fan, and W. Warsito, "Electrical capacitance volume tomography: Design and applications," *Sensors*, vol. 10, pp. 1890–1917, 2010.

[9] W. Gebrial, R. J. Prance, C. J. Harland, and T. D. Clark, "Non-invasive imaging using an array of electric potential sensors," *Review of Scientific Instruments*, vol. 77, pp. 063708–1, 2006.

[10] R. Banasiak, R. Wajman, D. Sankowski, and M. Soleimani, "Three-dimensional nonlinear inversion of electrical capacitance tomography data using a complete sensor model," *Progress in Electromagnetics Research*, vol. 100, pp. 219–234, 2010.

[11] S. Ren, F. Dong, Y. Xu, and C. Tan, "Reconstruction of the three-dimensional inclusion shapes using electrical capacitance tomography," *Measurement Science and Technology*, vol. 25, p. 025403, 2014.

[12] W. Q. Yang, D. M. Spink, J. C. Gamio, and M. S. Beck, "Sensitivity distributions of capacitance tomography sensors with parallel field excitation," *Meas. Sci. Technol.*, vol. 8, pp. 562–569, 1997.

[13] Q. Marashdeh and F. L. Teixeira, "Sensitivity matrix calculation for fast 3-d electrical capacitance tomography (ect) of flow systems," *IEEE TRANSACTIONS ON MAGNETICS*, vol. 40 (2), pp. 1204–1207, 2004.

[14] Y. S. Kim, S. H. Lee, U. Z. Ijaz, K. Y. Kim, and B. Y. Choi, "Sensitivity map generation in electrical capacitance tomography using mixed normalization models," *Meas. Sci. Technol.*, vol. 18, pp. 2092–2102, 2007.

[15] W. Q. Yang and L. Peng, "Image reconstruction algorithms for electrical capacitance tomography," *Meas. Sci. Technol.*, vol. 14, pp. R1–R13, 2003.

[16] A. Adler, J. H. Arnold, R. Bayford, A. Borsic, B. Brown, P. Dixon, T. J. C. Faes, I. Frerichs, H. Gagnon, Y. Garber, B. Grychtol, G. Hahn, W. R. B. Lionheart, A. Malik, R. P. Patterson, J. Stocks, A. Tizzard, N. Weiler, and G. K. Wolf, "Greit: a unified approach to 2d linear eit reconstruction of lung images," *Physiological Measurement*, vol. 30 (6), pp. S35–55, 2009.

[17] W. R. B. Lionheart, "Eit reconstruction algorithms: pitfalls, challenges and recent developments," *Physiological Measurement*, vol. 25, pp. 125–142, 2004.

[18] J. A. Scales, M. L. Smith, and S. Treitel, *Introductory Geophysical Inverse Theory, Section 5.04*. Samizdat Press, 2001.